Terahertz Emission from Anomalous Hall Effect in a Single-Layer Ferromagnet

Qi Zhang,[1,2] Ziyan Luo,[1] Hong Li,[2,3] Yumeng Yang,[1] Xinhai Zhang,[2,†] and Yihong Wu[1,*]

[1]*Department of Electrical and Computer Engineering, National University of Singapore, 4 Engineering Drive 3, Singapore 117583, Singapore*

[2]*Department of Electrical and Electronic Engineering, Southern University of Science and Technology, Xueyuan Rd 1088, Shenzhen 518055, China*

[3]*Institute of Applied Physics and Material Engineering, University of Macau, Avenida da Universidade, Macau 999078, China*

We report on terahertz (THz) emission from a single-layer ferromagnet, which involves the generation of backflow nonthermal charge current from the ferromagnet/dielectric interface by femtosecond laser excitation and subsequent conversion of the charge current to a transverse transient charge current via the anomalous Hall effect, thereby generating THz radiation. The THz emission can be either enhanced or suppressed or the polarity can be reversed by introducing a magnetization gradient in the thickness direction of the ferromagnet. Unlike spintronic THz emitters reported previously, it does not require an additional nonmagnetic layer or Rashba interface.

I. INTRODUCTION

Recently, spin-to-charge conversion in femtosecond- (fs) laser-excited magnetic heterostructures has attracted attention as a promising mechanism for producing terahertz (THz) waves with magnetically controllable polarization states [1]. The key to the THz emission is the generation of spin-polarized super-diffusive charge current from a ferromagnetic layer by fs laser excitation and subsequent conversion of the spin-polarized current to a transverse charge current by either inverse spin Hall effect (ISHE) [1–10] or inverse Rashba-Edelstein effect (IREE) [11–13]. The former involves a ferromagnet/nonmagnet (FM/NM) heterostructure wherein when a fs laser is irradiated on the FM/NM heterostructure, nonequilibrium electrons are excited to the states above the Fermi level, generating a super-diffusive spin-polarized current normal to the interface [14,15]. When the spin-polarized current enters the NM layer with large spin-orbit coupling (SOC), it is converted to a charge current in the transverse direction by ISHE, thereby generating the THz wave [1,2]. On the other hand, the THz emitter based on IREE typically consists of a FM with an adjacent Rashba interface, for example, FM/Ag/Bi [16]; in this case, the super-diffusive spin-polarized current launched by the FM layer is converted to a transverse charge current at the

*elewuyh@nus.edu.sg
†zhangxh@sustc.edu.cn

Ag/Bi interface via the IREE [11–13], which in the same way as the ISHE, generates the THz emission. In this letter, we examine the possibility of using the anomalous Hall effect (AHE) [17] to generate THz emission in a single-layer FM with a large SOC and demonstrate efficient THz emission in samples with a magnetization gradient.

As shown schematically in Fig. 1, when a thin metallic film is irradiated by a fs laser, the electrons are excited to states above the Fermi level [Fig. 1(a)]. Immediately after the excitation, equilibration takes place through two dominant mechanisms, that is, electron-electron and electron-phonon interactions [18]. Due to the much smaller heat capacity, the electron subsystem quickly reaches a high-temperature (T_e) Fermi-Dirac distribution within 0.1 ps [Fig. 1(b)], whereas the lattice stays close to the ambient temperature (T_p) [19]. The electrons subsequently cool and thermalize with their own lattice within a few picoseconds [Fig. 1(c)]. In addition to phonons, the magnon also plays a role in the equilibration process of hot electrons in ferromagnets. The magnon temperature (T_m) is typically higher than that of phonons before all three subsystems reach the thermal equilibrium [20,21].

Before the electron subsystem reaches the equilibrium (i.e., $t < 0.1$ ps), the nonthermal electrons move at a fast speed (approximately 10^6 m/s) in a super-diffusive manner [Fig. 1(d)] [14,15]. For electrons at a distance of at least a mean free path (λ_e) away from the top (e.g., with a MgO capping layer) and bottom (e.g., with a quartz substrate)
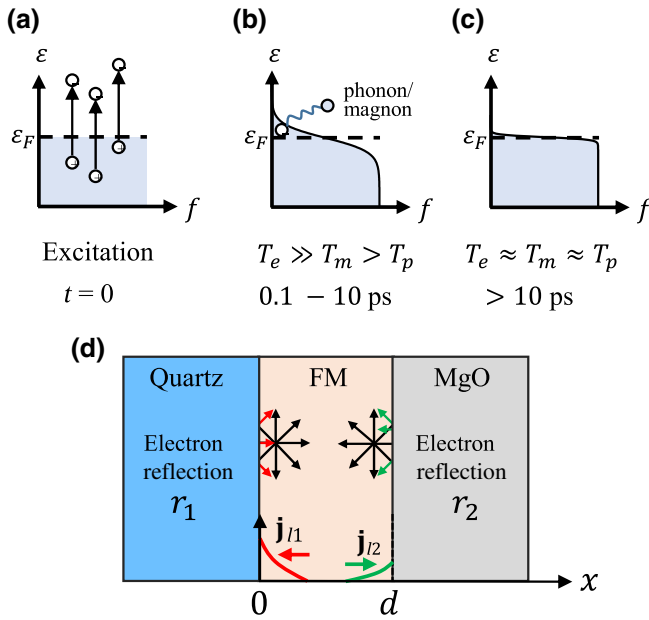
FIG. 1. (a)–(c) Subprocesses at different time scales after ultrafast laser excitation: (a) Excitation of nonequilibrium electrons. (b) High-temperature Fermi-Dirac distribution of electron subsystem. (c) Nearly thermal equilibrium state among electron, phonon, and magnon. (d) Schematic of nonthermal electron reflection at quartz/FM and FM/MgO interfaces and the formation of backflow current.

interfaces, they will collide with other electrons to reach the thermal equilibrium within the electron subsystem. However, for electrons with a distance shorter than λ_e from the interface, they will be reflected back to form a backflow current due to reflection at the FM/dielectric interface [15]. The amplitude of the backflow current depends strongly on the material properties and roughness of the interface. For metallic films deposited on a smooth substrate, the bottom interface will typically be smoother than the top interface. In this case, the backflow currents from the bottom ($\mathbf{j}_{l1}$) and ($\mathbf{j}_{l2}$) interfaces will not be completely cancelled out, leading to a net backflow current ($\mathbf{j}_{l1}$ - $\mathbf{j}_{l2}$). We argue that the backflow current will be converted to a transverse transient current when the FM has a large AHE. Recently, we have demonstrated that $(\mathrm{Fe_xMn_{1-x}})_y\mathrm{Pt_{1-y}}$ thin films with optimum compositions exhibit a sizable AHE, and the backflow of spin accumulation induced by the AHE gives the anomalous Hall magnetoresistance (AHMR) [22]. Here, we show that $(\mathrm{Fe_xMn_{1-x}})_y\mathrm{Pt_{1-y}}$ is also a promising material for an AHE-based THz emitter. We substantiate our arguments by examining both the thickness and pumping fluence dependence of the emission efficiency in $(\mathrm{Fe_xMn_{1-x}})_y\mathrm{Pt_{1-y}}$ emitters. We show that the use of a Pt composition gradient can either enhance or suppress the THz emission, depending on the gradient direction relative to the normal direction of the two interfaces.

II. EXPERIMENTAL RESULTS AND DISCUSSION

A. AHE origin of THz emission

The sample preparation and THz measurement methods are given in the Supplemental Material [23,24]. Figure 2(a) illustrates the THz generation from a fs-laser-pumped single-layer FM with either the quartz (up) or MgO (down) side pumping. We first measure the THz emission from a $(\mathrm{Fe_{0.8}Mn_{0.2}})_{0.67}\mathrm{Pt_{0.33}}$ (3) thin film capped by MgO (4) (hereafter the number inside the brackets indicates film thickness in nm), and the results are shown in Fig. 2(b), where the upper and lower pair of waveforms are obtained from the quartz side and MgO side pumping at a fluence of 555 $\mu\mathrm{J/cm^2}$, respectively. The solid and dashed lines correspond to the applied field in the $+y$ and $-y$ directions, respectively. It is apparent that the THz polarity is reversed when either the applied magnetic field or the pumping direction is reversed; the former indicates that the THz emission is of magnetic origin [25–27] whereas the latter implies that there is a reversal of the sign of the driving force that is responsible for the generation of the THz wave. Similar sign dependence on pumping direction has been observed in FM/NM bilayer emitters [2,6,8]. But, in those cases, it is understood that the sign reversal of THz wave polarization is caused by the reversal of the direction of spin-polarized current due to sample flipping [3,10]. In the present case, however, there is only a thin layer of FM; the flipping of the sample will not break the symmetry as long as the sample is homogenous in the thickness direction, which is presumably the present case. Therefore, the most likely cause for the sign reversal is the presence of a net longitudinal current in the film thickness direction as discussed above. With the presence of AHE, the longitudinal current is converted to a transient transverse current $\mathbf{j}_t = \theta_{\mathrm{AHE}}\mathbf{m} \times \mathbf{j}_l$ with $\mathbf{m}$ the magnetization direction, $\mathbf{j}_l$ the net longitudinal current, and θ_{AHE} the AHE angle. Since $\mathbf{j}_l$ is physically related to two interfaces, the reverse of the pumping direction, that is, sample flipping, will lead to the sign reversal of $\mathbf{j}_l$. This explains why the polarity of THz reverses when either the pumping direction or magnetization direction is reversed. In addition to $(\mathrm{Fe_{0.8}Mn_{0.2}})_{0.67}\mathrm{Pt_{0.33}}$, we also conduct similar experiments by replacing $(\mathrm{Fe_{0.8}Mn_{0.2}})_{0.67}\mathrm{Pt_{0.33}}$ with $\mathrm{Fe_{0.8}Mn_{0.2}}$ (3), $\mathrm{Co_{0.2}Fe_{0.6}B_{0.2}}$ (3), and $\mathrm{Ni_{0.8}Fe_{0.2}}$ (3) while the rest remains the same. Indeed, we observe THz radiations from all the three samples, though their amplitudes are much smaller compared to that of $(\mathrm{Fe_{0.8}Mn_{0.2}})_{0.67}\mathrm{Pt_{0.33}}$. Interestingly, the polarity of the THz wave also reverses when either the pumping direction or the magnetic field direction is reversed for all the samples. We plot the peak values of THz waveforms of the four emitters in Fig. 2(c) with a positive magnetic field. The positive (negative) values correspond to quartz (MgO) side pumping. The $\mathrm{Ni_{0.8}Fe_{0.2}}$ shows a larger amplitude compared to $\mathrm{Fe_{0.8}Mn_{0.2}}$ and $\mathrm{Co_{0.2}Fe_{0.6}B_{0.2}}$, which is in agreement with the observation
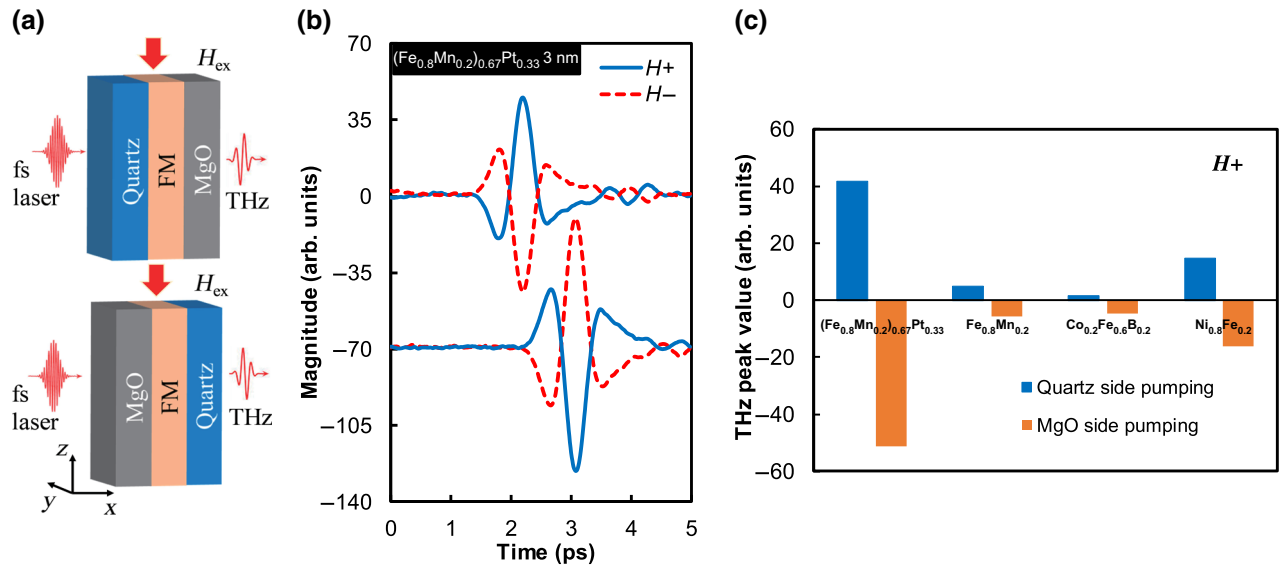
FIG. 2. (a) Schematics of THz emission setup with pumping from the quartz (up) and MgO (down) sides, respectively. (b) THz wave from $(Fe_{0.8}Mn_{0.2})_{0.67}Pt_{0.33}$. The upper pair of waveforms is from the quartz side pumping and the lower pair is from the MgO side pumping. Solid and dashed lines correspond to positive and negative fields, respectively. (c) THz peak values from different emitters: $(Fe_{0.8}Mn_{0.2})_{0.67}Pt_{0.33}$, $Fe_{0.8}Mn_{0.2}$, $Co_{0.2}Fe_{0.6}B_{0.2}$, and $Ni_{0.8}Fe_{0.2}$, with positive applied H field (positive amplitude, quartz side pumping; negative amplitude, MgO side pumping).

of a larger AHE in $Ni_{0.8}Fe_{0.2}$ [28–30], though the roughness of the interface may also play a role. The above results provide strong evidence that the THz emission from $(Fe_{0.8}Mn_{0.2})_{0.67}Pt_{0.33}$ originates from the AHE.

B. Thickness dependence of THz emission

To further test the relevance of the proposed AHE origin, we study the thickness dependence of THz emission from single-layer $(Fe_{0.8}Mn_{0.2})_{0.67}Pt_{0.33}$ from 3 to 9 nm. Figures 3(a) and 3(b) show the emission waveforms (shifted along the time axis for clarity) and the

corresponding peak amplitude (symbol), respectively. As can be seen, the THz amplitude increases from 3 to 4 nm and then decreases monotonically as the thickness increases further, with a broad maximum at around 4 nm. The thickness dependence can be modeled by involving the following subprocesses: (i) generation of nonequilibrium electrons by laser excitation, (ii) generation of backflow current at the two interfaces, (iii) creation of transverse transient charge current via AHE, and (iv) conversion of the charge current to THz emission. Without losing generality, we assume that the electron reflection coefficients at the quartz/FM and FM/MgO interfaces are
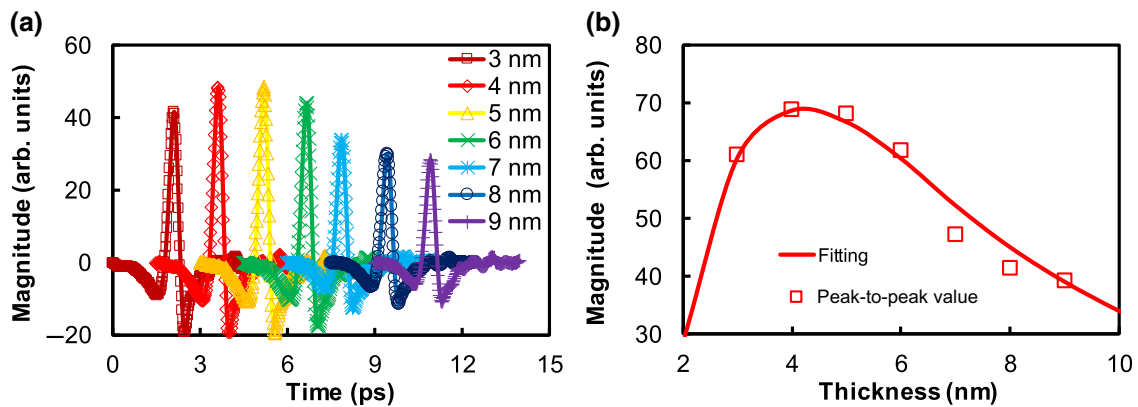

FIG. 3. Thickness dependence of THz waveform from $(Fe_{0.8}Mn_{0.2})_{0.67}Pt_{0.33}$ single-layer FM emitter: (a) THz waveform at different $(Fe_{0.8}Mn_{0.2})_{0.67}Pt_{0.33}$ thicknesses (shifted in time axis for clarity). (b) Peak-to-peak THz amplitude as a function of thickness [symbol, measured data; solid line, fitting using Eq. (1)].

r_1 and r_2, respectively [Fig. 1(d)]. We also assume that the resulting superdiffusive current decays exponentially from the two interfaces. Based on this model, the electric field of the THz emission may be written as

$$
\begin{aligned}
E_{\text{THz}} &\propto M_s(d) \cdot FA(d)v_e(d) \cdot \int_0^d \theta_{\text{AHE}}(r_1 e^{-[x/(\lambda_e/2)]} \\
&\quad \times e^{-[(d-x)/\lambda_T]} - r_2 e^{(x-d)/(\lambda_e/2)} e^{-[(d-x)/(\lambda_T)]})dx \\
&\quad \times \frac{1}{n_{\text{air}} + n_{\text{sub}} + Z_0\sigma d} \\
&= M_s(d) \cdot FA(d)v_e(d) \cdot \theta_{\text{AHE}}[r_1\lambda_1 e^{-(d/\lambda_T)} \\
&\quad \times (1 - e^{-(d/\lambda_1)}) - r_2\lambda_2(1 - e^{-(d/\lambda_2)})] \\
&\quad \times \frac{1}{n_{\text{air}} + n_{\text{sub}} + Z_0\sigma d}
\end{aligned}
\tag{1}
$$

where d is the FM thickness, F is the fluence, $A(d)$ is the absorptance of the FM layer, r_1 and r_2 are the reflection coefficients at two interfaces, λ_e is the nonequilibrium electron mean free path, λ_T is the decay length of THz emission inside the FM layer, $v_e(d)$ is the average electron speed, $M_s(d)$ is the saturation magnetization, $n_{\text{air}}(n_{\text{sub}})$ is the reflective index of air (substrate), Z_0 is the impedance of free space, and $\lambda_1 = (\lambda_e\lambda_T/2)/(\lambda_T - \lambda_e/2)$, $\lambda_2 = (\lambda_e\lambda_T/2)/(\lambda_T + \lambda_e/2)$. Here, we have included the explicit thickness dependence of A, v_e, and M_s in the equation. $A(d)$ is obtained from fitting to the experimental data, which yields $A(d) = 0.0314d + 0.1767$ (with d in nm). $v_e(d)$ is estimated from the electron temperature (T_e), which itself is related to the absorbed laser energy per unit volume (E_a) [31,32]: $E_a = \xi(T_e^2 - T_0^2)/2$, where ξ is the electronic specific heat and T_0 is the initial electron temperature (i.e., room temperature). Substituting $E_a = A(d)F/d$ into the previous equation, one obtains $v_e \propto \sqrt{T_e} = [(2A(d) \cdot F/\xi d) + T_0^2]^{1/4}$, where F is the laser fluence. In addition to A and v_e, the saturation magnetization also depends on d, which drops quickly with reducing d when $d < 5$ nm, as revealed in our previous study [22]. A polynomial fitting to the experimental data is used to calculate E_{THz} in Eq. (1) (see the Supplemental Material [23]). The first and second terms in the integrand of Eq. (1) represent the longitudinal to transverse current conversion efficiency as well as the small absorption of the THz wave by the metal layer near the two interfaces. The last term of Eq. (1) denotes the transverse current to THz conversion efficiency. As shown by the solid line in Fig. 3(b), the thickness dependence of the THz peak amplitude can be fitted well using Eq. (1) with the following parameters: $\lambda_e = 1.2$ nm, $\lambda_T = 14$ nm, $r_1 = 0.6$, $r_2 = 0.1$ (see the Supplemental Material for more details [23]), $F = 555$ μJ/cm^2 (experimental value), $\xi = 0.7$ mJ/cm^{3}K^2, $n_{\text{air}} = 1$, $n_{\text{sub}} = 1.453$, $Z_0 = 377$ Ω, and

$\sigma = 5.32 \times 10^6$ S $\cdot$ m^{-1}. As the electron specific heat of $(Fe_{0.8}Mn_{0.2})_{0.67}Pt_{0.33}$ is not available, we use the reported value for Fe [32] instead. Assuming every single photon excites an electron-hole pair at an absorptance of 0.4, a laser beam with a fluence of $F = 555$ μJ/cm^2 will lead to a nonthermal electron density of about 0.88 nm^{-3}, which is equivalent to an average electron spacing of 1.05 nm. Therefore, the fitted value of $\lambda_e = 1.2$ nm is reasonable. The fitted THz decay length of 14 nm is comparable to the reported value in FM/NM bilayers [8]. The conductivity of 5.32×10^6 S$\cdot$m^{-1} is obtained experimentally for the 9-nm $(Fe_{0.8}Mn_{0.2})_{0.67}Pt_{0.33}$ [22]. The good agreement between fitted and measured thickness dependences provides further support of the proposed AHE origin of THz emission.

C. Pump fluence dependence of THz emission

Next, we discuss the pumping fluence dependence of THz radiation from the $(Fe_{0.8}Mn_{0.2})_{0.67}Pt_{0.33}$ (d) emitters as shown in Fig. 4. The symbols denote the measured values and solid lines are fitting curves according to Eq. (1). At a fluence of 555 μJ/cm^2, $\lambda_1 \approx \lambda_2 \approx (\lambda_e/2) = 0.6$ nm. Therefore, the fluence dependence of E_{THz} is mainly determined by $M_sFv_e\lambda_e$ and the last term of Eq. (1) with $v_e \propto (A(d)/\xi d)^{1/4}(F + \Gamma)^{1/4}$ where $\Gamma = (\xi d)/[2A(d)]$ (note: $T_e \gg T_0$) and $\lambda_e \propto [A(d)F]^{-1/3}$. The laser-heating-induced magnetization reduction may be approximated by $M_s(d) = M_{s0}(d)[1 - \gamma(T_e - T_0)]$, where $M_{s0}(d)$ is the saturation magnetization at T_0 and γ is a thickness-dependent constant. It is thickness dependent because the temperature dependence of magnetization is different at different thicknesses when d is small. As shown in Fig. 4, the experimental results can be fitted very well using Eq. (1) by treating γ as a thickness-dependent fitting parameter. The inset shows the thickness dependence of γ
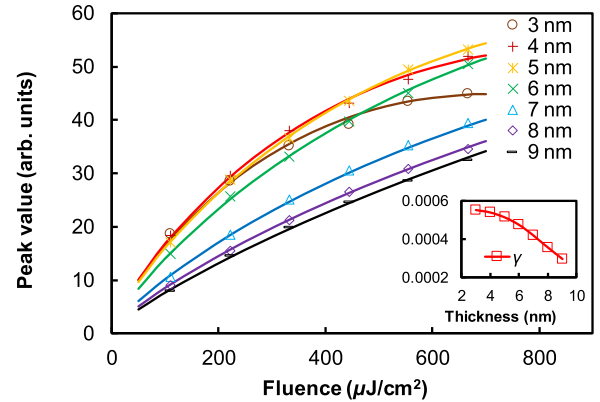

FIG. 4. Pumping fluence dependence of THz peak amplitude from the $(Fe_{0.8}Mn_{0.2})_{0.67}Pt_{0.33}$ single-layer FM emitter: Peak amplitude as a function of fluence for emitters with different $(Fe_{0.8}Mn_{0.2})_{0.67}Pt_{0.33}$ thickness. Inset: coefficient (γ) of laser heating effect on saturation magnetization.
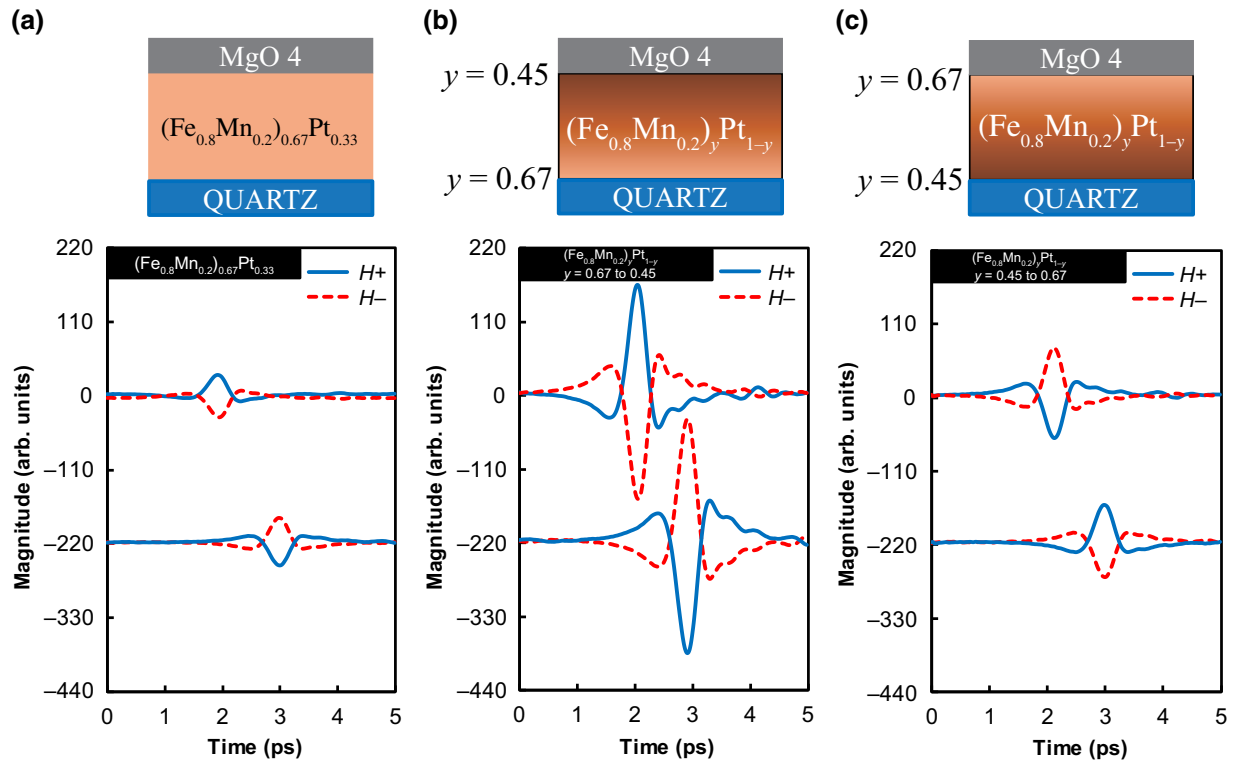
FIG. 5.   (a) THz emission from $(Fe_{0.8}Mn_{0.2})_{0.67}Pt_{0.33}$ with uniform Pt composition. (b) THz emission from $(Fe_{0.8}Mn_{0.2})_y Pt_{1-y}$ with positive Pt composition gradient, i.e., y varies from 0.67 (bottom) to 0.45 (top). (c) THz emission from $(Fe_{0.8}Mn_{0.2})_y Pt_{1-y}$ with negative Pt composition gradient, i.e., y varies from 0.45 (bottom) to 0.67 (top). In all the figures, the upper pair of waveforms is from quartz side pumping and the lower pair is from MgO side pumping. Solid and dashed lines correspond to positive and negative fields, respectively. Darker color indicates the region with higher Pt composition. All the films have a thickness of 9 nm.

used in the fitting. As expected, γ decreases with increasing d as the heating effect becomes weaker at larger thicknesses (see more discussion in the Supplemental Material [23]) [33–35].

III. ENHANCEMENT OF TERAHERTZ EMISSION USING GRADED COMPOSITION LAYER

With the confirmation of AHE origin, now we discuss how we can enhance the THz emission. An obvious approach is to optimize the Pt composition in order to increase the difference between AHE near the two interfaces, thereby increasing the THz efficiency. As discussed in the Supplemental Material [23], at a thickness of 3 nm, the THz peak-to-peak amplitude ratios of $(Fe_{0.8}Mn_{0.2})_y Pt_{1-y}$ emitters deposited at Pt powers of 15 ($y = 0.67$), 35 ($y = 0.52$), and 50 ($y = 0.45$) W are 14.1:1.7:1, with the sample deposited at 15 W showing the strongest THz emission. This prompts us to introduce a Pt gradient in the thickness direction. When the film is irradiated by a laser, immediately after the laser excitation, the spin polarization of the nonequilibrium electrons is assumed to be the same as those in the equilibrium state at Fermi level [14]. Therefore, the Pt composition gradient

will be converted to a spin chemical potential gradient $\nabla \boldsymbol{\mu}_s$ in the thickness direction [20,36]. With the presence of $\nabla \boldsymbol{\mu}_s$, the total transverse current may be written as $\mathbf{j}_t = \theta_{AHE}\mathbf{m} \times \mathbf{j}_{bf} + \theta_{SHE}\sigma \mathbf{s} \times \nabla(\boldsymbol{\mu}_s/2e)$, where θ_{SHE} is the spin Hall angle, $\mathbf{s}$ is the net spin polarization direction of nonequilibrium electrons, and $\boldsymbol{\mu}_s$ is the spin chemical potential [37,38]. Therefore, the introduction of the Pt composition gradient may either enhance or reduce the THz emission, depending on the sign of $\nabla \boldsymbol{\mu}_s$ and relative contributions from the two terms.

Figure 5(a) shows the THz waveform from $(Fe_{0.8}Mn_{0.2})_{0.67}Pt_{0.33}$ (9) with uniform Pt composition (15 W), which is almost the same as that of $(Fe_{0.8}Mn_{0.2})_{0.67}Pt_{0.33}$ (3) shown in Fig. 2(b). Figure 5(b) shows THz emission from $(Fe_{0.8}Mn_{0.2})_y Pt_{1-y}$ (9) with a positive Pt gradient (i.e., y varies from 0.67 (bottom) to 0.45 (top).). Compared to the waveform shown in Fig. 5(a), the polarity remains the same but the peak-to-peak amplitude is increased by a factor of 5.4 (212 versus 39 in arbitrary units). This means that a positive Pt composition gradient helps to enhance the THz emission. On the other hand, as shown in Fig. 5(c), the sample with a negative Pt composition gradient (i.e., y varies from 0.45 (bottom) to 0.67 (top).) gives a much smaller THz signal with a peak-to-peak amplitude of -84.

The negative sign indicates that the polarity is reversed compared to the previous two cases. The ratio of the peak-to-peak amplitudes of the three samples is 1:5.4:−2.15. If we simply estimate the peak-to-peak amplitude ratio of the three samples by using $r_1 = 0.6$, $r_2 = 0.1$, and the amplitude ratio from the samples with a uniform Pt composition as discussed above, the ratio of these samples turns out to be 1:1.18:−0.11. Obviously, the two sets of values do not tally, suggesting that the magnetization gradient plays an important role. The discrepancy can be resolved by taking into account the contribution from $\nabla \boldsymbol{\mu}_s$, as discussed in the Supplemental Material [23]. These results demonstrate that the spin chemical potential gradient plays an important role in THz emission from the single-layer FM. With further optimization of the materials and composition gradient, the current approach can potentially lead to more efficient THz emission.

IV. CONCLUSIONS

In summary, we demonstrate an alternative mechanism for generating THz emission from an ultrathin FM layer via the AHE, though the presence of AHE in the THz regime has been reported before [39–41]. The process involves generation of backflow superdiffusive current at the FM/dielectric interfaces and subsequent conversion of the charge current to transverse current via AHE, thereby generating the THz radiation. The THz generation is mainly caused by the nonthermal superdiffusive current near the two interfaces; the contribution from laser-excitation-induced hot carrier gradient inside the sample, if any, should be very small considering the large effective penetration depth (see the Supplemental Material [23]) compared to the film thickness [42]. Further investigations can be carried out in the future using multiple wavelength excitations when the laser sources are available [43,44]. There is tremendous room for improvement of emission efficiency once materials with large AHEs are found. In the meantime, as we demonstrate in this paper, the emission efficiency can also be enhanced by introducing a gradient in the FM magnetization.

ACKNOWLEDGMENTS

[1] T. Kampfrath, M. Battiato, P. Maldonado, G. Eilers, J. Nötzold, S. Mährlein, V. Zbarsky, F. Freimuth, Y. Mokrousov, S. Blügel, M. Wolf, I. Radu, P. M. Oppeneer, and M. Münzenberg, Terahertz spin current pulses controlled by magnetic heterostructures, Nat. Nanotechnol. **8,** 256 (2013).

[2] T. Seifert, et al., Efficient metallic spintronic emitters of ultrabroadband terahertz radiation, Nat. Photonics **10,** 483 (2016).

[3] T. J. Huisman, R. V. Mikhaylovskiy, J. D. Costa, F. Freimuth, E. Paz, J. Ventura, P. P. Freitas, S. Blügel, Y. Mokrousov, Th. Rasing, and A. V. Kimel, Femtosecond control of electric currents in metallic ferromagnetic heterostructures, Nat. Nanotechnol. **11,** 455 (2016).

[4] D. Yang, J. Liang, C. Zhou, L. Sun, R. Zheng, S. Luo, Y. Wu, and J. Qi, Powerful and tunable THz emitters based on the Fe/Pt magnetic heterostructure, Adv. Opt. Mater. **4,** 1944 (2016).

[5] T. Seifert, S. Jaiswal, M. Sajadi, G. Jakob, S. Winnerl, M. Wolf, M. Kläui, and T. Kampfrath, Ultrabroadband single-cycle terahertz pulses with peak fields of 300 kV cm^{-1} from a metallic spintronic emitter, Appl. Phys. Lett. **110,** 252402 (2017).

[6] Y. Wu, M. Elyasi, X. Qiu, M. Chen, Y. Liu, L. Ke, and H. Yang, High-performance THz emitters based on ferromagnetic/nonmagnetic heterostructures, Adv. Mater. **29,** 1603031 (2017).

[7] S. Zhang, Z. Jin, Z. Zhu, W. Zhu, Z. Zhang, G. Ma, and J. Yao, Bursts of efficient terahertz radiation with saturation effect from metal-based ferromagnetic heterostructures, J. Phys. D: Appl. Phys. **51,** 034001 (2018).

[8] G. Torosyan, S. Keller, L. Scheuer, R. Beigang, and E. T. Papaioannou, Optimized spintronic terahertz emitters based on epitaxial grown Fe/Pt layer structures, Sci. Rep. **8,** 1311 (2018).

[9] M. Chen, R. Mishra, Y. Wu, K. Lee, and H. Yang, Terahertz emission from compensated magnetic heterostructures, Adv. Opt. Mater. **6,** 1800430 (2018).

[10] H. S. Qiu, K. Kato, K. Hirota, N. Sarukura, M. Yoshimura, and M. Nakajima, Layer thickness dependence of the terahertz emission based on spin current in ferromagnetic heterostructures, Opt. Express **26,** 15247 (2018).

[11] J. C. R. Sánchez, L. Vila, G. Desfonds, S. Gambarelli, J. P. Attané, J. M. De Teresa, C. Magén, and A. Fert, Spin-to-charge conversion using Rashba coupling at the interface between non-magnetic materials, Nat. Commun. **4,** 2944 (2013).

[12] M. B. Jungfleisch, Q. Zhang, W. Zhang, J. E. Pearson, R. D. Schaller, H. Wen, and A. Hoffmann, Control of Terahertz Emission by Ultrafast Spin-Charge Current Conversion at Rashba Interfaces, Phys. Rev. Lett. **120,** 207207 (2018).

[13] C. Zhou, Y. P. Liu, Z. Wang, S. J. Ma, M. W. Jia, R. Q. Wu, L. Zhou, W. Zhang, M. K. Liu, Y. Z. Wu, and J. Qi, Broadband Terahertz Generation via the Interface Inverse Rashba-Edelstein Effect, Phys. Rev. Lett. **121,** 086801 (2018).

[14] M. Battiato, K. Carva, and P. M. Oppeneer, Superdiffusive spin transport as a mechanism of ultrafast demagnetization, Phys. Rev. Lett. **105,** 027203 (2010).

[15] M. Battiato, K. Carva, and P. M. Oppeneer, Theory of laser-induced ultrafast superdiffusive spin transport in layered heterostructures, Phys. Rev. B **86,** 024404 (2012).

[16] C. R. Ast, J. Henk, A. Ernst, L. Moreschini, M. C. Falub, D. Pacilé, P. Bruno, K. Kern, and M. Grioni, Giant Spin

Splitting through Surface Alloying, Phys. Rev. Lett. **98,** 186807 (2007).

[17] N. Nagaosa, J. Sinova, S. Onoda, A. H. MacDonald, and N. P. Ong, Anomalous hall effect, Rev. Mod. Phys. **82,** 1539 (2010).

[18] R. H. M. Groeneveld, R. Sprik, and A. Lagendijk, Femtosecond spectroscopy of electron-electron and electron-phonon energy relaxation in Ag and Au, Phys. Rev. B **51,** 11433 (1995).

[19] B. Rethfeld, A. Kaiser, M. Vicanek, and G. Simon, Ultrafast dynamics of nonequilibrium electrons in metals under femtosecond laser irradiation, Phys. Rev. B **65,** 214303 (2002).

[20] I. H. Shin, B. C. Min, B. K. Ju, and G. M. Choi, Ultrafast spin current generated by electron–magnon scattering in bulk of ferromagnets, Jpn. J. Appl. Phys. **57,** 090307 (2018).

[21] M. Schreier, A. Kamra, M. Weiler, J. Xiao, G. E. W. Bauer, R. Gross, and S. T. B. Goennenwein, Magnon, phonon, and electron temperature profiles and the spin Seebeck effect in magnetic insulator/normal metal hybrid structures, Phys. Rev. B **88,** 094410 (2013).

[22] Y. Yang, Z. Luo, H. Wu, Y. Xu, R. W. Li, S. J. Pennycook, S. Zhang, and Y. Wu, Anomalous Hall magnetoresistance in a ferromagnet, Nat. Commun. **9,** 2255 (2018).

[23] See Supplemental Material at http://link.aps.org/supplemental/10.1103/PhysRevApplied.12.054027 for details on the sample preparation and THz measurement methods, thickness dependence of saturation magnetization of FeMnPt, THz emission from thick FM emitter, temperature dependence of magnetization, dependence of AHE on Pt sputtering power, discussion on the THz emission from FeMnPt with a Pt gradient, THz emission from MgO/FM/MgO symmetric sample and estimation of magnetic dipole radiation.

[24] P. C. M. Planken, C. E. W. M. v. Rijmenam, and R. N. Schouten, Opto-electronic pulsed THz systems, Semicond. Sci. Technol. **20,** S121 (2005).

[25] E. Beaurepaire, G. M. Turner, S. M. Harrel, M. C. Beard, J. Y. Bigot, and C. A. Schmuttenmaer, Coherent terahertz emission from ferromagnetic films excited by femtosecond laser pulses, Appl. Phys. Lett. **84,** 3465 (2004).

[26] T. J. Huisman, R. V. Mikhaylovskiy, A. Tsukamoto, Th. Rasing, and A. V. Kimel, Simultaneous measurements of terahertz emission and magneto-optical Kerr effect for resolving ultrafast laser-induced demagnetization dynamics, Phys. Rev. B **92,** 104419 (2015).

[27] S. Zhang, Z. Jin, X. Liu, W. Zhao, X. Lin, C. Jing, and G. Ma, Photoinduced terahertz radiation and negative conductivity dynamics in Heusler alloy Co_2MnSn film, Opt. Lett. **42,** 3080 (2017).

[28] Y. Q. Zhang, N. Y. Sun, R. Shan, J. W. Zhang, S. M. Zhou, Z. Shi, and G. Y. Guo, Anomalous Hall effect in epitaxial permalloy thin films, J. Appl. Phys. **114,** 163714 (2013).

[29] T. Taniguchi, J. Grollier, and M. D. Stiles, Spin-Transfer Torques Generated by the Anomalous Hall Effect and Anisotropic Magnetoresistance, Phys. Rev. Appl. **3,** 044001 (2015).

[30] L. L. Lang, S. M. Zhou, W. J. Fan, and X. P. Qiu, Anomalous Hall magnetoresistance in metastable antiferromagnetic FeMn, AIP Adv. **8,** 125220 (2018).

[31] S. Mondal and A. Barman, Laser Controlled Spin Dynamics of Ferromagnetic Thin Film from Femtosecond to Nanosecond Timescale, Phys. Rev. Appl. **10,** 054037 (2018).

[32] E. Carpene, E. Mancini, C. Dallera, M. Brenna, E. Puppin, and S. De Silvestri, Dynamics of electron-magnon interaction and ultrafast demagnetization in thin iron films, Phys. Rev. B **78,** 174422 (2008).

[33] M. D. Kuz'min, Shape of Temperature Dependence of Spontaneous Magnetization of Ferromagnets: Quantitative Analysis, Phys. Rev. Lett. **94,** 107204 (2005).

[34] M. D. Kuz'min, M. Richter, and A. N. Yaresko, Factors determining the shape of the temperature dependence of the spontaneous magnetization of a ferromagnet, Phys. Rev. B **73,** 100401(R) (2006).

[35] J. C. Le Guillou and J. Zinn-Justin, Critical Exponents for the *n*-Vector Model in Three Dimensions from Field Theory, Phys. Rev. Lett. **39,** 95 (1977).

[36] T. S. Seifert, et al., Femtosecond formation dynamics of the spin Seebeck effect revealed by terahertz spectroscopy, Nat. Commun. **9,** 2899 (2018).

[37] A. Popescu, P. Rodriguez-Lopez, P. M. Haney, and L. M. Woods, Thermally driven anomalous Hall effect transitions in FeRh, Phys. Rev. B **97,** 140407(R) (2018).

[38] C. Fang, C. H. Wan, Z. H. Yuan, L. Huang, X. Zhang, H. Wu, Q. T. Zhang, and X. F. Han, Scaling relation between anomalous Nernst and Hall effect in $[Pt/Co]_n$ multilayers, Phys. Rev. B **93,** 054420(R) (2016).

[39] C. B. Schmidt, S. Priyadarshi, and M. Bieler, Subpicosecond temporal resolution of anomalous Hall currents in GaAs, Sci. Rep. **7,** 11241 (2017).

[40] R. Shimano, Y. Ikebe, K. S. Takahashi, M. Kawasaki, N. Nagaosa, and Y. Tokura, Terahertz Faraday rotation induced by an anomalous Hall effect in the itinerant ferromagnet $SrRuO_3$, EPL (Europhysics Letters) **95,** 17002 (2011).

[41] T. J. Huisman, R. V. Mikhaylovskiy, Th. Rasing, A. V. Kimel, A. Tsukamoto, B. de Ronde, L. Ma, W. J. Fan, and S. M. Zhou, Sub-100-ps dynamics of the anomalous Hall effect at terahertz frequencies, Phys. Rev. B **95,** 094418 (2017).

[42] J. Hohlfeld, S. S. Wellershoff, J. Güdde, U. Conrad, V. Jähnke, and E. Matthias, Electron and lattice dynamics following optical excitation of metals, Chem. Phys. **251,** 237 (2000).

[43] E. T. Papaioannou, G. Torosyan, S. Keller, L. Scheuer, M. Battiato, V. K. Mag-Usara, J. L'huillier, M. Tani, and R. Beigang, Efficient terahertz generation using Fe/Pt spintronic emitters pumped at different wavelengths, IEEE Trans. Magn. **54,** 9100205 (2018).

[44] R. I. Herapath, S. M. Hornett, T. S. Seifert, G. Jakob, M. Kläui, J. Bertolotti, T. Kampfrath, and E. Hendry, Impact of pump wavelength on terahertz emission of a cavity-enhanced spintronic trilayer, Appl. Phys. Lett. **114,** 041107 (2019).